PCCP

ROYAL SOCIETY OF CHEMISTRY

PAPER

Published on 05 November 2026
Licence and permissions

Check for updates

Cite this: DOI: 10.1039/d6cp02133f

Mode-resolved vibronic control of excited-state dynamics in multi-resonance TADF emitters

Sanyam * and Anirban Mondal *

Multi-resonance thermally activated delayed fluorescence (MR-TADF) emitters are among the most promising candidates for next-generation narrowband organic light-emitting diodes (OLEDs). However, despite their rigid frameworks and exceptional optoelectronic performance, the role of nuclear vibrations in governing their excited-state dynamics remains insufficiently understood. In particular, the mode-specific vibrational contributions to internal conversion (IC), intersystem crossing (ISC), and reverse intersystem crossing (RISC) have not been systematically established for MR-TADF systems. Here, we address this gap through a comprehensive mode-resolved computational investigation of four prototypical MR-TADF emitters: **DABNA-1**, **PXZ-BN**, **DTBA-BN2**, and **TAZ-BN**. By quantifying Huang–Rhys factors, electron–phonon coupling strengths, and vibrationally resolved non-radiative rate contributions, we uncover a clear vibronic partitioning of the relaxation pathways. Low-frequency delocalized modes predominantly drive IC losses, whereas selected high-frequency localized vibrations play a decisive role in promoting RISC. Among the molecules studied, **DTBA-BN2** exhibits the most favorable balance between suppressed non-radiative decay, efficient triplet upconversion, and strong radiative emission. Furthermore, comparison between fully quantum-mechanical and semiclassical Marcus treatments identifies the reorganization-energy regime in which semiclassical approximations remain reliable for MR-TADF emitters. These findings establish fundamental vibronic design principles and provide practical descriptors for the rational development of high-efficiency, narrowband MR-TADF materials.

Received 5th June 2026,
Accepted 4th November 2026

DOI: 10.1039/d6cp02133f

rsc.li/pccp

1 Introduction

Thermally activated delayed fluorescence (TADF) emitters have recently emerged as some of the most promising candidates for organic light-emitting diodes (OLEDs) and advanced display technologies.[1–4] Their ability to harvest both singlet and triplet excitons enables nearly complete exciton utilization, significantly enhancing device efficiency. As a result, TADF-based OLEDs can deliver improved brightness, high contrast ratios, and enhanced energy efficiency in display applications.[5–7] In addition, the purely organic nature of these materials allows their optoelectronic properties to be tuned through rational molecular design, where functional group substitution and structural modifications provide versatile control over emission characteristics.[8–10]

From a molecular design perspective, maximizing exciton utilization requires simultaneously achieving efficient fluorescence (k_R) and reverse intersystem crossing (k_{RISC}) rates.[11–13] The efficiencies of these processes depend on a delicate balance among several key parameters, including the rates of intersystem crossing (ISC) and reverse intersystem crossing (RISC), the magnitude of spin–orbit coupling (SOC), and the singlet–triplet energy gap (ΔE_{ST}). These quantities are strongly governed by the electronic structure of the emitter and its chemical composition.[14–19]

Beyond purely electronic factors, vibrational effects also play a critical role in determining excited-state relaxation pathways. Although the Born–Oppenheimer approximation treats nuclear motion as slower than electronic motion, energy redistribution through molecular vibrations—such as stretching, bending, and out-of-plane motions—can significantly influence nonradiative decay and excited-state dynamics.[20–22] In conventional donor–acceptor (D–A) molecular architectures, flexible single bonds and conformational freedom introduce numerous vibrational degrees of freedom that can enhance nonradiative relaxation pathways and reduce emission efficiency.[23] Previous studies on representative D–A systems have shown that specific vibrational modes can strongly modulate radiative and nonradiative processes, thereby influencing overall device performance.[20–22,24]

In contrast, multi-resonant thermally activated delayed fluorescence (MR-TADF) emitters possess rigid and highly planar molecular frameworks that restrict conformational motion and suppress structural disorder. Such rigidity is generally believed to reduce vibrationally induced nonradiative losses, contributing to their narrow emission spectra and high

Department of Chemistry, Indian Institute of Technology Gandhinagar, Gujarat, 382355, India. E-mail: sanyamsanyam@iitgn.ac.in, amondal@iitgn.ac.in

photoluminescence quantum yields. However, despite these structural advantages, significant variations in device performance are still observed among MR-TADF emitters with closely related molecular frameworks. This suggests that factors beyond conventional electronic descriptors may influence their excited-state dynamics.[25–28]

Recent studies have highlighted that the coupling between vibrational motion and electronic transitions—often described through the Herzberg–Teller effect and exciton–phonon interactions—can play an important role in governing emission processes.[20–24] For example, investigations of radical-based emitters demonstrated that detrimental vibrational modes can be effectively decoupled from electronic transitions to improve performance.[21] Similarly, studies on inverted singlet–triplet gap (INVEST) emitters have shown that certain vibrational modes can constructively facilitate emission through enhanced vibronic coupling.[23] These findings suggest that vibrational effects are not universally detrimental but may play a nuanced role in determining the photophysical behavior of emissive materials. Nevertheless, a detailed understanding of how specific vibrational modes influence the excited-state dynamics of structurally rigid MR-TADF emitters remains largely unexplored.

To address this question, we performed a comprehensive computational investigation of four representative MR-TADF emitters—**DABNA-1**, **PXZ-BN**, **DTBA-BN2**, and **TAZ-BN**—(Fig. 1)—previously synthesized and experimentally characterized in the literature.[8,29–33] Although these molecules share closely related multi-resonant frameworks, their optoelectronic performances differ substantially. By combining excited-state electronic structure analysis with detailed vibrational mode characterization, we systematically evaluated the contributions of Huang–Rhys (HR) factors, exciton–phonon coupling, and vibronic interactions to the key photophysical processes governing emission. Our analysis reveals that vibrational modes do not universally degrade molecular performance; instead, certain modes can actively enhance reverse intersystem crossing and thereby improve delayed fluorescence efficiency. By establishing correlations between vibrational characteristics, molecular structure, and photophysical rates, this study provides new insights into the role of vibronic effects in MR-TADF emitters and offers practical guidance for the rational design of next-generation OLED materials.

2 Methods

As stated above, this study focuses on four representative MR-TADF emitters—**DABNA-1**, **PXZ-BN**, **DTBA-BN2**, and **TAZ-BN**—whose molecular structures are shown in Fig. 1.[8,29–33] These molecules share a common multi-resonant core framework but differ in the nature of their fused and substituted ring fragments, which ultimately influence their photophysical behavior. Specifically, **DABNA-1** contains phenyl substituents, **PXZ-BN** incorporates fused phenoxazine (PXZ) units, **DTBA-BN2** features Dithienyltribenzo[*b*,*d*,*f*]azepine (*i.e.*, two fuzed 7-membered rings), and similarly, **TAZ-BN** also includes three 7-membered nitrogen-containing azapine moieties. Moreover for clarity the IUPAC names (or formal names in case of more complex compounds) have been mentioned in the Table S1 in the SI. Although the underlying MR framework remains preserved across the series, these structural variations lead to noticeable differences in experimentally measured properties, including the singlet–triplet energy gap and external quantum efficiency, as summarized in Table S2.

The presence of distinct structural fragments—such as phenyl rings, fused cyclic units, carbazole-like motifs, and larger nitrogen-containing seven-membered rings—modulates the electronic structure and consequently affects the efficiency of TADF processes. At the same time, these structural modifications alter the overall molecular size and vibrational landscape of the emitters. As a result, the four molecules exhibit different numbers of vibrational modes: **DABNA-1**, **PXZ-BN**, **DTBA-BN2**, and **TAZ-BN** have 150, 144, 198, and 252 modes, respectively. These variations can significantly influence vibrational dynamics and the associated excited-state relaxation processes. While the synthesis and experimental characterization of these MR-TADF emitters have been reported previously, the present study aims to provide detailed molecular-level insights into the origins of the distinct photophysical behaviors observed among these structurally related systems.

All quantum-chemical calculations were carried out using the Gaussian 09 software package and the ORCA 5.0 program suite.[34,35] Molecular structures and vibrational normal modes were visualized using GaussView. Ground-state geometries were optimized within the framework of density functional theory (DFT) employing the PBE1PBE functional[36] together with the def2-TZV basis set. Harmonic vibrational frequency

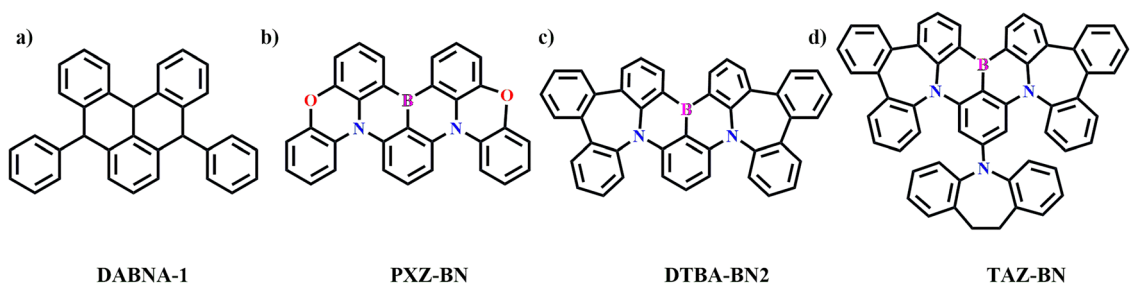


Fig. 1 Chemical structures of the four MR-TADF emitters investigated in this study: (a) **DABNA-1**, (b) **PXZ-BN**, (c) **DTBA-BN2**, and (d) **TAZ-BN**. These molecules share a multi-resonant core framework but differ in their fused and substituted ring fragments.

 This journal is © the Owner Societies 2026

calculations were subsequently performed to verify that each optimized structure corresponds to a true minimum on the potential energy surface, as confirmed by the absence of imaginary frequencies. Moreover, our primary objective is to analyze the vibrational frequencies rather than to predict the ΔE_{ST}. Therefore, the PBE1PBE/def2-TZV level of theory provides a reasonable and computationally efficient choice.[37,38] In addition, this methodology has already been employed successfully in several recent studies.[23,24]

Conventional hybrid functionals such as PBE1PBE have recognized limitations in quantitatively describing excited-state charge-transfer (CT) energetics and multiresonance excitation energies compared with high-level wavefunction methods (*e.g.*, STEOM-DLPNO-CCSD); however, the primary objective of this study is to characterize the potential energy surfaces, vibrational normal modes, and nuclear displacements governing excited-state relaxation. PBE1PBE offers a practical balance between computational efficiency and accuracy for geometry optimizations and harmonic frequency calculations.[24,39,40] This distinction is critical because the central conclusions of this work—including mode-resolved contributions to non-radiative relaxation, internal conversion, and spin-vibronic coupling—depend on the fidelity of the calculated vibrational modes and nuclear displacements rather than the absolute accuracy of the electronic energy gaps. Furthermore, recent systematic benchmarks on thermally activated delayed fluorescence (TADF) emitters demonstrate that dispersion-corrected global hybrid functionals provide ground- and excited-state geometries, singlet–triplet gaps, and photophysical rate constants comparable to those obtained with computationally demanding, optimally tuned range-separated functionals.[41]

To explicitly evaluate the performance of PBE1PBE for the systems studied here, we compared its results with those obtained using the M06-2X functional for a representative molecule, **DABNA-1**, as shown in Fig. S1(a–d). M06-2X is a global hybrid functional featuring a high fraction of Hartree–Fock exchange (54%), which has been shown to yield improved accuracy for excited-state energetics and potential energy surfaces in systems with significant charge-transfer character.[42] The optimized geometries exhibit excellent overall agreement (Fig. S1(a)), with the PBE1PBE and M06-2X structures shown in blue and red, respectively. The molecular core remains virtually identical, with minor structural deviations confined to peripheral substituents. Both functionals also yield consistent vibrational frequencies and normal mode compositions (Fig. S1(b)). Furthermore, the density difference plots (DDPs) reveal nearly identical charge-redistribution patterns upon excitation (Fig. S1(c and d)), where blue and yellow regions denote increases and decreases in electron density, respectively.

To further quantify the electronic nature of the lowest singlet excited state, we evaluated the charge-transfer (CT) number (Q_{CT}), CT distance (D_{CT}), and overlap integral between the hole and electron distributions ($S^{\pm}$). PBE1PBE yields values of Q_{CT} = 0.58, D_{CT} = 1.54 Å, and $S^{\pm}$ = 0.92, while M06-2X yields Q_{CT} = 0.56, D_{CT} = 1.32 Å, and $S^{\pm}$ = 0.94. The close agreement between these parameters confirms that both functionals describe a consistent, short-range charge-transfer profile for the excited state.[43] Taken together, these structural, vibrational, and electronic comparisons demonstrate that PBE1PBE reliably captures the qualitative and quantitative features required to model vibrationally mediated excited-state relaxation in **DABNA-1**. Given that the remaining molecules in this study share closely related structural motifs, extending the use of PBE1PBE across the dataset is methodologically sound within the scope of this investigation.

Excited-state geometry optimizations were then carried out using ORCA 5.0. Based on the optimized S_1 geometries, the lowest three singlet and triplet excitation energies were calculated. Solvent effects were incorporated using the conductor-like polarizable continuum model (CPCM) with toluene as the solvent.[44] Following the optimization of both ground- and excited-state structures (singlet and triplet), additional frequency calculations were performed. The resulting outputs were used to evaluate Huang–Rhys factors, electron–phonon coupling constants, and mode-resolved reorganization energies, which form the basis for analyzing the radiative and non-radiative decay processes in these systems.[21]

The Huang–Rhys factor associated with a vibrational mode k is related to the electron–phonon coupling $V_{ev(i)}(k)$ through

$$S_i(k) = \left[\frac{V_{ev(i)}(k)}{\hbar\omega_k}\right]^2, \tag{1}$$

where $S_i(k)$ denotes the HR factor of the kth vibrational mode and ω_k represents the corresponding vibrational frequency. The vibrational reorganization energy is then obtained by summing the contributions from all vibrational modes,

$$\lambda_v = \sum_k \hbar\omega_k S_i(k), \tag{2}$$

where λ_v represents the total vibrational reorganization energy arising from mode-resolved electron–phonon coupling.

After determining the reorganization energies and electron–phonon coupling constants, the mode-specific non-radiative decay rates were evaluated using

$$k_{nr} = \frac{C^2\sqrt{2\pi}}{\hbar\sqrt{\hbar\omega\Delta E}}\exp\left[-\frac{\Delta E}{\hbar\omega}\left\{\ln\left(\frac{\Delta E}{\sum_i \lambda_i}\right) - 1\right\}\right], \tag{3}$$

where C denotes the effective electronic coupling matrix element, ω is the frequency of the accepting vibrational mode, and ΔE represents the energy gap between the initial and final electronic states. The term $\sum_i \lambda_i$ corresponds to the total reorganization energy arising from all contributing vibrational modes. This formulation allows a quantitative evaluation of the contribution of individual vibrational modes to the overall non-radiative decay process.

To complement the above analysis, the reverse intersystem crossing rate was evaluated using both the semiclassical Marcus framework and a fully quantum-mechanical

treatment. Within the Marcus formalism, the RISC rate is given by

$$k_{\mathrm{RISC}}^{\mathrm{M}} = \frac{2\pi}{\hbar} \frac{\left| H_{\mathrm{SO}}^{\mathrm{S_1T_1}} \right|^2}{\sqrt{4\pi\lambda k_{\mathrm{B}} T}} \exp\left[-\frac{(\Delta E_{\mathrm{ST}} + \lambda)^2}{4\lambda k_{\mathrm{B}} T} \right], \qquad (4)$$

where λ denotes the total reorganization energy associated with the $S_1 \leftrightarrow T_1$ transition, T is the temperature, $H_{\mathrm{SO}}^{\mathrm{S_1T_1}}$ represents the spin–orbit coupling matrix element, and ΔE_{ST} is the singlet–triplet energy gap.[45]

In addition to the semiclassical description, the RISC rate was also evaluated using the fully quantum-mechanical framework proposed by Troisi *et al.*[22] This approach enables a direct comparison between the Marcus-based semiclassical expression and the full quantum treatment of vibronic coupling. Such a comparison provides insights into the regimes of ΔE_{ST} and λ for which the semiclassical approximation remains valid and where quantum-mechanical effects become significant. Further details on the implementation of the quantum-mechanical rate calculations are provided in Section S1 of the SI.

3 Results and discussion

As mentioned earlier, the experimentally determined photophysical parameters of the investigated compounds are summarized in Table S2. In this work, we aim to elucidate how individual vibrational modes influence emitter performance, either by promoting non-radiative decay pathways or by enhancing photophysical efficiency through increased reverse intersystem crossing rates. To achieve this, we performed a mode-resolved analysis by evaluating the Huang–Rhys factors, followed by the corresponding vibronic couplings and non-radiative decay rates for each vibrational mode. Furthermore, to establish the correspondence between vibrational mode numbers and their associated frequencies, the mode-mapping data are provided in Fig. S2, together with the corresponding infrared (IR) spectra shown in Fig. S3.

To delineate the origin of the observed photophysical differences, it is necessary to decouple electronic framework effects from mode-specific vibronic influences. While embedded heteroatoms (O, N) dictate electronic parameters such as π-conjugation, oscillator strength (f), and ΔE_{ST}, their constrained placement in rigid rings limits their direct impact on the low-frequency vibrational landscape. Instead, variations in ring topology—such as 6- *versus* 7-membered fused units—governs the spatial distribution and density of normal modes. Mode-resolved Huang–Rhys analysis reveals that non-radiative losses in **DABNA-1** and **PXZ-BN** are predominantly governed by ring-size-dependent vibronic coupling. In contrast, the performance differences between **DTBA-BN2** and **TAZ-BN** arise primarily from variations in electronic structure (specifically oscillator strength and orbital overlap) rather than from vibrational dynamics alone. Thus, our proposed vibronic design principles generally apply to non-radiative decay control, while radiative rates remain inherently tied to the electronic symmetry of the specific MR framework.

Fig. 2 presents the mode-resolved distribution of the Huang–Rhys factors for the four investigated molecules using a polar representation. In this visualization, the angular coordinate corresponds to the vibrational mode number, while the radial distance represents the magnitude of the HR factor on a logarithmic scale. The different-colored markers denote the three relevant non-radiative electronic transitions considered in this work: internal conversion (IC) from S_1 to S_0, intersystem crossing (ISC) from S_1 to T_1, and reverse intersystem crossing (RISC) from T_1 to S_1. Since the HR factor is directly related to the mode-specific reorganization energy, this analysis provides a quantitative description of how individual vibrational modes contribute to the overall excited-state relaxation dynamics.

As evident from Fig. 2, the HR factors systematically decrease with increasing vibrational mode number, reflected by the progressive contraction of the radial distribution at higher modes. This trend indicates that low-frequency vibrations, which require lower excitation energies, are comparatively more delocalized in nature, whereas high-frequency modes become increasingly localized on specific molecular fragments. Importantly, this behavior is consistently observed across all four investigated emitters, suggesting that such mode-dependent vibronic characteristics are intrinsic to rigid MR-TADF frameworks.

The polar representation also clearly highlights the selective participation of specific vibrational modes in the different relaxation channels. In particular, the IC pathways exhibit a substantially broader radial distribution, indicating larger HR factors and stronger nuclear reorganization. In contrast, the ISC and RISC channels remain comparatively confined to lower HR values. This distinction already suggests that fundamentally different vibronic landscapes govern spin-allowed and spin-forbidden processes. For completeness, the corresponding mode-specific reorganization energies are provided in Fig. S4. Because the reorganization energy is directly determined by the combined contributions of the Huang–Rhys factors and the electron–phonon coupling strengths, we focus here on discussing these fundamental quantities explicitly, while the resulting reorganization energy distributions are included in the SI.

These differences in the vibrational distributions can be further understood by considering the fundamental nature of the underlying electronic transitions. Internal conversion occurs between electronic states of identical spin multiplicity and is therefore typically associated with comparatively larger energy gaps and stronger nuclear relaxation effects. In contrast, intersystem crossing and reverse ISC involve spin-forbidden transitions between singlet and triplet manifolds and generally proceed with much smaller energy changes. Nevertheless, all three processes are accompanied by geometric relaxation as the molecule evolves from the initial to the final electronic state. The resulting structural rearrangements are directly reflected in the HR factors, which quantify the extent of nuclear reorganization associated with each transition.

As shown in Fig. 2a–d, the IC pathways (red markers) consistently exhibit substantially larger HR factors than the corresponding ISC (blue markers) and RISC (yellow markers) channels. This behavior indicates that IC is accompanied by

 This journal is © the Owner Societies 2026

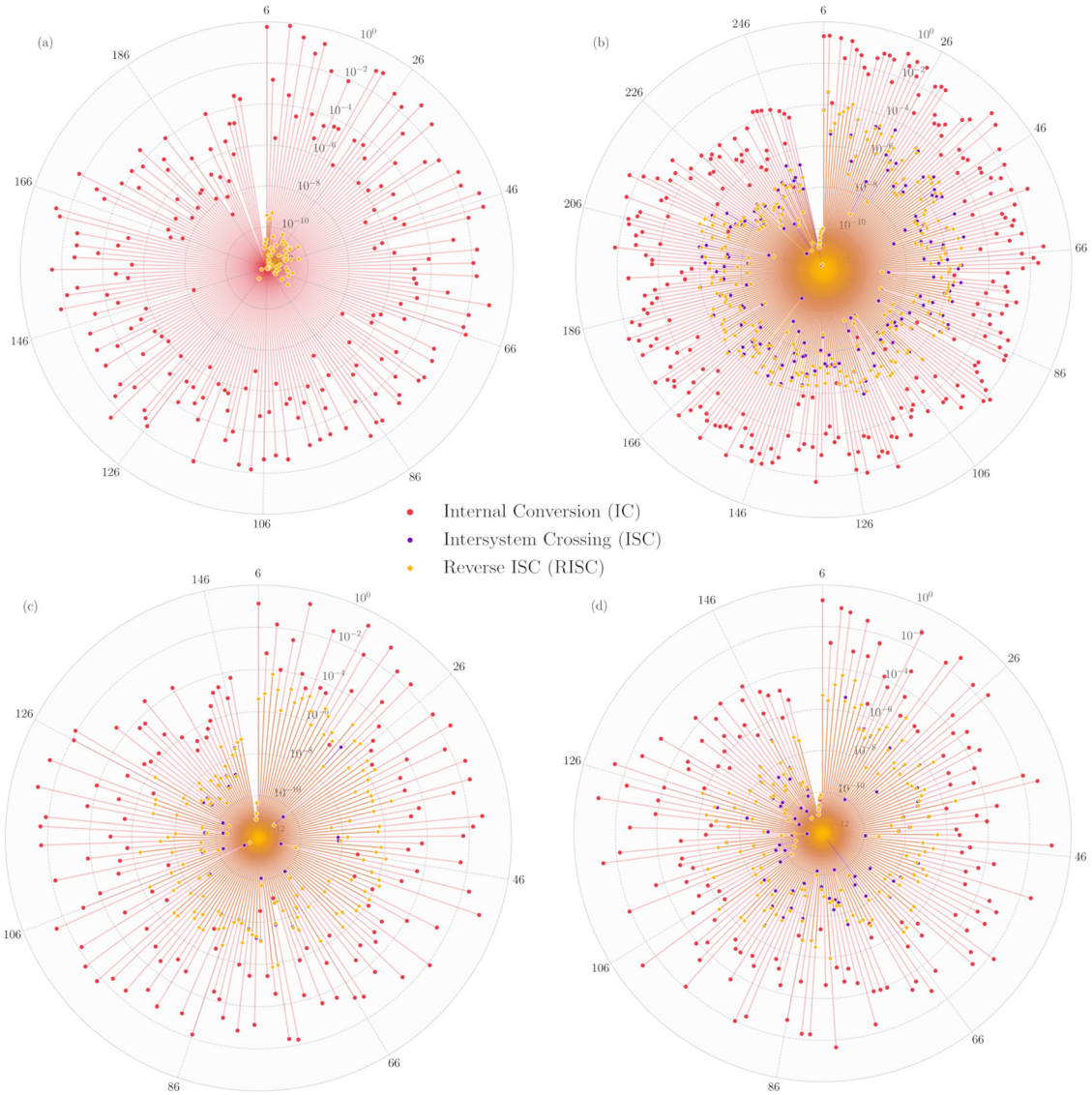


Fig. 2 Mode-resolved distribution of the Huang–Rhys factors (S) for internal conversion (IC, red), intersystem crossing (ISC, dark blue), and reverse intersystem crossing (RISC, orange) pathways in (a) **DTBA-BN2**, (b) **TAZ-BN**, (c) **PXZ-BN**, and (d) **DABNA-1**, respectively. The radial axis maps the magnitude of the electron-vibrational coupling on a logarithmic scale ($1\log_{10}S$), spans from 10^{-15} to 10^{0}, while the angular axis corresponds to individual vibrational mode numbers. Solid stems and geometric markers indicate the specific contributions of discrete vibrational frequencies to non-radiative deactivation and spin–flip processes, highlighting the dominant ''vibrational gatekeepers'' that modulate the exciton-harvesting dynamics.

significantly larger reorganization energies and greater nuclear displacement between the participating electronic states. In contrast, the comparatively smaller HR factors associated with ISC and RISC reflect weaker structural distortion and more delocalized vibrational participation during these spin-forbidden transitions, conditions that are generally favorable for efficient excited-state interconversion. Having established the distinct vibronic characteristics of the IC, ISC, and RISC processes, we next examine how these vibrational features correlate with the experimentally observed emission efficiencies of the investigated MR-TADF emitters. As summarized in Table S2, the external quantum efficiency (EQE) follows the trend **DTBA-BN2** > **TAZ-BN** > **PXZ-BN** > **DABNA-1**.

If vibrational dynamics play a decisive role in determining emitter performance, highly efficient systems would be expected to possess fewer vibrational modes that contribute significantly to the total reorganization energy, thereby suppressing energy dissipation through non-radiative channels. Conversely, less efficient emitters should display larger HR factors and a greater density of vibrationally active modes. It should also be noted that the total number of vibrational modes differs among the four molecules, namely **TAZ-BN** (252), **DTBA-BN2** (198), **DABNA-1** (150), and **PXZ-BN** (144), as discussed in the Methodology section. Despite these differences in molecular size and vibrational dimensionality, several clear and systematic trends emerge from the mode-resolved analysis.

Focusing first on the IC transition, all four molecules exhibit a large population of vibrational modes with HR factors below 10^{-6}, indicating highly localized vibrations that contribute negligibly to the total reorganization energy. Among the investigated emitters, **DTBA-BN2** (Fig. 2a), which shows the highest experimental efficiency, possesses a markedly larger number of modes with HR factors below 10^{-4} compared to the other molecules. This behavior suggests that most vibrational modes in **DTBA-BN2** couple only weakly to the electronic transition, thereby minimizing nuclear reorganization and suppressing non-radiative energy dissipation. An even more striking feature is observed for the ISC and RISC channels of **DTBA-BN2**, where the HR factors remain extremely small and highly localized. In fact, the ISC and RISC distributions almost completely overlap, with the blue ISC markers largely hidden beneath the yellow RISC markers because of their nearly identical magnitudes and the stronger visual contrast of the latter.

In contrast, **TAZ-BN**, the second-best-performing emitter, exhibits a noticeably larger population of low-frequency vibrational modes, particularly below mode number 50, with HR factors exceeding 10^{-3} (Fig. 2b). This behavior indicates stronger vibrational distortions and greater nuclear participation, which may partially limit its emissive performance. Similar trends are observed for **PXZ-BN** and **DABNA-1** (Fig. 2c and d), both of which display progressively larger vibrational contributions, consistent with their comparatively lower experimental efficiencies. Because direct comparison of individual vibrational modes across different molecules is inherently challenging, we introduce two global descriptors: the effective Huang–Rhys factor (S_{eff}) and the effective vibrational frequency (ν_{eff}), whose definitions are provided in the SI (eqn (S1) and (S2)). The corresponding values are summarized in Table 1. Since S_{eff} represents the cumulative sum of all mode-specific HR factors, it provides an overall measure of the extent of vibrational participation in a given transition.

Interestingly, **DTBA-BN2** exhibits the largest S_{eff} for the IC process, which is likely a consequence of its comparatively large number of vibrational modes. However, for both ISC and RISC, **DTBA-BN2** shows the smallest S_{eff} values among all four molecules, despite possessing more vibrational modes than **PXZ-BN** and **DABNA-1**. This observation is particularly significant because it demonstrates that the total number of vibrational modes alone does not determine vibronic activity; rather, the decisive factor is the strength of coupling between those modes and the relevant electronic transitions. Equally noteworthy is that the second-lowest S_{eff} for ISC and RISC does not correspond to **TAZ-BN**. The remaining molecules exhibit S_{eff} values on the order of 10^{-4}, reflecting comparatively stronger overall vibrational participation in the spin-forbidden channels.

Furthermore, the effective HR factors for IC are substantially larger than those for ISC and RISC across all molecules, fully consistent with the stronger nuclear reorganization associated with same-spin internal conversion. Overall, these results establish the Huang–Rhys factor as a robust descriptor for correlating vibrational dynamics with non-radiative relaxation pathways. At the same time, HR factors alone do not provide the complete picture; mode-specific electron–phonon coupling strengths and the resulting non-radiative rate constants must also be considered to fully understand the excited-state dynamics and emission efficiencies of these MR-TADF emitters.

To evaluate the predictive capability of S_{eff}, ν_{eff}, and mode-resolved vibronic spectra, we examined their correlations with experimental PLQY, peak EQE, and k_{RISC} (Fig. S5 of SI). The ratio of the effective frequency factor to the Huang–Rhys factor ($\nu_{\mathrm{eff}}/S_{\mathrm{eff}}$) exhibits a clear linear correlation with experimental device EQE, demonstrating that suppressing effective vibrational frequency factors reduces non-radiative dissipation and enhances overall device efficiency. While higher k_{RISC} generally drives improvements in both PLQY and EQE by accelerating triplet harvesting, the correlation with PLQY deviates at the lowest-performing emitter (**DABNA-1**). This deviation illustrates that high RISC rates alone do not guarantee maximum PLQY; performance is ultimately dictated by the competition between radiative emission (k_{r}), spin–flip dynamics (k_{RISC}), and non-radiative decay channels (k_{IC}). Thus, while $\nu_{\mathrm{eff}}/S_{\mathrm{eff}}$ serves as a powerful linear screening descriptor for device trends, comprehensive prediction of prospective MR-TADF materials requires evaluating S_{eff}, ν_{eff}, k_{RISC}, and k_{IC} as an integrated descriptor set.

Next, we evaluated the mode-specific electron–phonon couplings together with the corresponding mode-specific non-radiative transition rates in order to directly correlate vibronic couplings with their vibrational modes as shown in Fig. 3. As it is evident from the Fig. 3, the horizontal axis corresponds to the logarithm of electron–phonon couplings, while the vertical axis represents the logarithm of the mode-specific transition rate. The color scale denotes the vibrational mode number.

Overall, a clear correlation emerges between the electron–phonon coupling strengths and the corresponding mode-specific transition rates. Vibrational modes with stronger couplings generally exhibit higher transition rates, confirming that strong vibronic interactions are the primary driving force behind non-radiative relaxation. At the same time, the transition rates are not

Table 1 Summary of the effective Huang–Rhys factors (S_{eff}), effective vibrational frequencies (ν_{eff}), and corresponding non-radiative decay rates (k_{nr}) for the internal conversion (IC), intersystem crossing (ISC), and reverse intersystem crossing (RISC) processes of the investigated MR-TADF emitters

	S_{eff}			ν_{eff} (cm^{-1})			k_{nr} (10^4 s^{-1})		
Molecule	IC	ISC	RISC	IC	ISC	RISC	IC	ISC	RISC
DTBA-BN2	2.88	2.15×10^{-9}	2.15×10^{-9}	320	295	296	1.39	1.89×10^{-4}	1.89×10^{-4}
TAZ-BN	2.43	1.14×10^{-3}	1.11×10^{-3}	347	192	172	1.05	77.41	46.13
PXZ-BN	1.40	1.98×10^{-4}	1.98×10^{-4}	569	279	279	0.59	0.031	0.030
DABNA-1	1.12	1.52×10^{-4}	1.51×10^{-4}	653	265	266	0.01	0.012	0.012

This journal is © the Owner Societies 2026

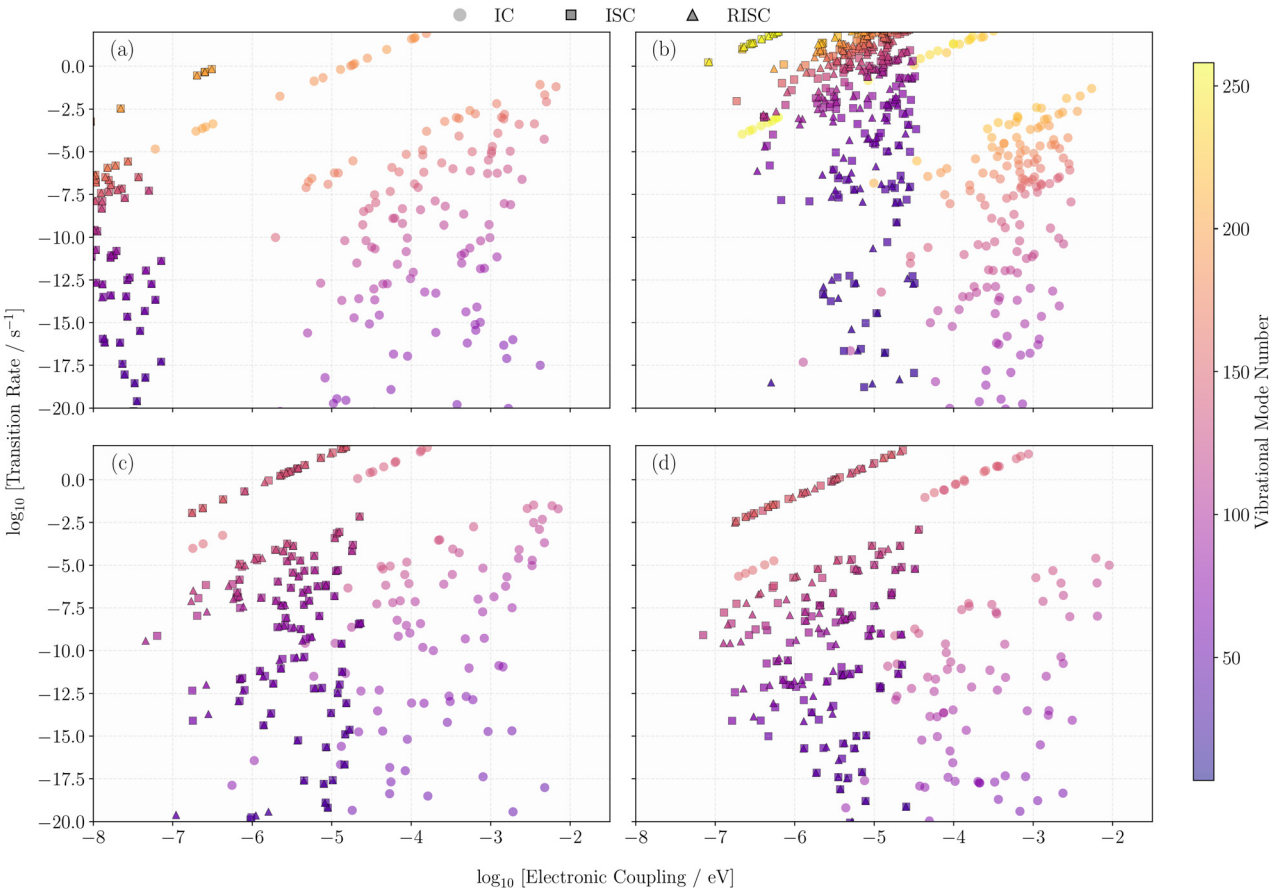


Fig. 3 Vibronic coupling-rate phase space mapping for the primary non-radiative and spin–flip pathways across four representative thermally activated delayed fluorescence systems: (a) **DTBA-BN2**, (b) **TAZ-BN**, (c) **PXZ-BN**, and (d) **DABNA-1**. Transition rates are plotted against their corresponding electronic coupling matrix elements across all active vibrational modes. Geometric markers distinguish the electronic transition processes: circles (○) denote internal conversion (IC, $S_1 \rightarrow S_0$), squares (□) represent intersystem crossing (ISC, $S_1 \rightarrow T_1$), and triangles (Δ) indicate reverse intersystem crossing (RISC, $T_1 \rightarrow S_1$). The color coding maps the vibrational mode number on a uniform global scale, enabling direct comparative visualization of how low-frequency skeletal vibrations *versus* high-frequency local modes govern the competing photophysical rates and overall exciton-harvesting efficiencies.

determined solely by the coupling magnitude. The vibrational frequency and energy gap for the transition also play important roles, leading certain high-frequency modes to contribute disproportionately, despite relatively moderate coupling strengths. Consequently, the dominant vibronic activity (higher coupling values) across the series is concentrated primarily in the low- to intermediate-frequency vibrational region, approximately corresponding to mode number 50 to 150 for **DTBA-BN2** and **TAZ-BN**, and for **PXZ-BN** and **DABNA-1** from 50 to 125 and covers a frequency range 500–1600 cm^{-1}. These modes mainly originate from skeletal stretching and in-plane/out-of-plane bending motions of the fused aromatic framework, which efficiently perturb the π-electron density during excited-state relaxation.

The influence of spin multiplicity on vibronic coupling strengths is immediately evident from Fig. 3. For all four emitters, the IC channels consistently exhibit substantially larger coupling magnitudes than the corresponding ISC and RISC processes. This behavior is fully consistent with the spin-allowed nature of IC transitions, where population transfer occurs between electronic states of identical multiplicity. In contrast, ISC and RISC involve a change in spin multiplicity and therefore require simultaneous participation of spin–orbit coupling and vibrational motion to mediate the formally forbidden transitions. As a result, the ISC/RISC coupling strengths are significantly attenuated, often reaching values several orders of magnitude smaller than those associated with IC. This reduction is directly reflected in the corresponding mode-specific transition rates, which are generally much smaller for ISC and RISC than for IC.

A molecule-wise examination reveals substantial differences in the vibronic landscapes of the four emitters. **DTBA-BN2** (Fig. 3a) exhibits highly localized vibronic characteristics (as seen from HR factors), but if we see coupling-wise, the same is also the case. The IC process is dominated by a single vibrational mode with relatively strong coupling (more than 0.006 eV), whereas the ISC and RISC channels remain extremely weak. Most of the ISC/RISC contributions are clustered near coupling strengths of approximately 10^{-7}–10^{-6} eV, with transition rates extending down to nearly 10^{-20} s^{-1}. Interestingly, unlike the other emitters, **DTBA-BN2** displays appreciable ISC/RISC contributions from high-frequency vibrational modes, as reflected by the larger mode numbers associated with several

square and triangular data points highlighted in yellow. In particular, the strongest coupled mode corresponds to mode 204 at 3199 cm^{-1} (Fig. 4a), indicating that high-frequency C–H stretching vibrations contribute significantly to the spin–flip dynamics in this system. This unusual behavior suggests a highly specialized vibronic environment governing the triplet-to-singlet upconversion pathway.

TAZ-BN (Fig. 3b) displays a markedly different behavior. In contrast to **DTBA-BN2**, both ISC and RISC exhibit substantially stronger coupling strengths and correspondingly enhanced mode-specific transition rates. Indeed, the ISC/RISC rates in **TAZ-BN** become comparable to, and in some regions even exceed, the IC contributions due to least singlet–triplet gap (0.03 eV) together with the presence of the additional seven-membered ring and the extended conjugated framework, both of which promote vibrational delocalization and mode mixing. The dominant vibronic activity is concentrated in the intermediate-frequency region, particularly for vibrational modes associated with skeletal distortions of the extended fused-ring framework. The strongest coupled mode appears near 1615 cm^{-1} (Fig. 4b), indicating that collective in-plane stretching motions efficiently facilitate spin-vibronic mixing.

PXZ-BN (Fig. 3c) also exhibits an intermediate vibronic profile between the highly localized **DTBA-BN2** and the strongly mixed **TAZ-BN** system. Compared to **DTBA-BN2** and **TAZ-BN**, **PXZ-BN** exhibits a broader distribution of IC-active vibrational modes, suggesting a richer vibronic manifold that contributes to internal conversion. Multiple modes simultaneously exhibit moderate coupling strengths and non-radiative contributions, suggesting a more delocalized vibrational relaxation network. The dominant coupled mode appears at a comparatively low frequency of 389.2 cm^{-1} (Fig. 4c), implying that low-frequency torsional or out-of-plane vibrational motions play a significant role in facilitating spin-vibronic coupling in this emitter. Although the ISC/RISC coupling strengths remain weaker than those observed for **TAZ-BN**, they are substantially larger than those in **DTBA-BN2**, resulting in moderate spin–flip transition efficiencies.

DABNA-1 (Fig. 3d) exhibits a comparatively similar vibronic profile as **PXZ-BN** because of a similar singlet–triplet gap and a similar molecular architecture (absence of 7-membered rings). Both the IC and ISC/RISC channels display relatively distributed vibrational contributions, although the overall IC activity remains somewhat weaker than in **PXZ-BN**. Similar to **TAZ-BN**, the strongest coupled mode is centered near 1615 cm^{-1} (Fig. 4d), reflecting the importance of collective aromatic skeletal vibrations in mediating spin-vibronic coupling.

The integrated representation in Fig. 3 illustrates the important relationship between vibrational mode number and non-radiative activity. Generally, higher-frequency modes exhibit larger mode-specific transition rates, a trend particularly pronounced in IC processes. This observation aligns with the energy-gap law: high-frequency vibrations effectively bridge electronic states by enhancing the overlap of vibrational wavefunctions. However, efficient transition pathways do not strictly necessitate maximum coupling strengths. Indeed, several modes with moderate electron–phonon coupling contribute significantly to the total transition rates due to favorable vibrational energetics. Consequently, the observed non-radiative behavior results from a complex interplay among coupling magnitude, vibrational frequency, mode delocalization, and the energetic alignment of the involved electronic states. Further mode-specific analysis, detailed in Fig. S5 and S6, identifies the visualization of vibrations with the highest RISC and IC transition rates. Notably, the most

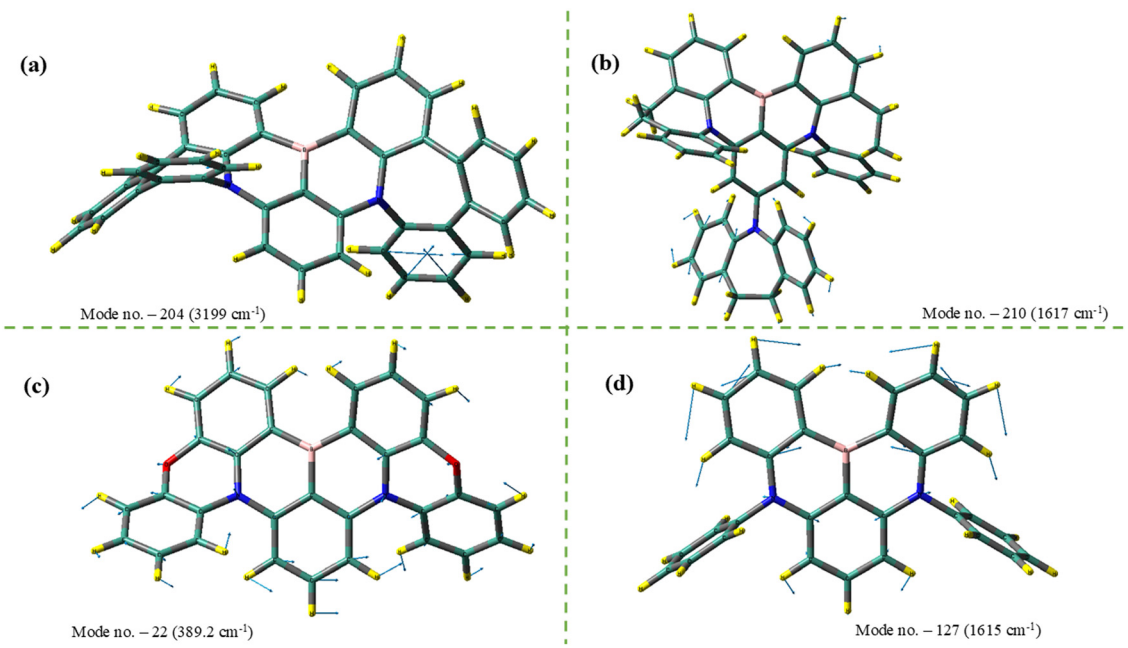


Fig. 4 Visualization of the dominant vibrational modes exhibiting the strongest electron–phonon coupling contributions to the RISC process in the investigated MR-TADF emitters: (a) **DTBA-BN2**, (b) **TAZ-BN**, (c) **PXZ-BN**, and (d) **DABNA-1**.

This journal is © the Owner Societies 2026

active modes for IC/RISC transitions generally differ from those with the highest coupling strengths, except for **DTBA-BN2**. In all investigated systems, these dominant modes are identified as C–H stretching vibrations, occurring in both symmetric and asymmetric stretchings.

A distinct regioselective dependence is observed for these high-rate modes. For **DTBA-BN2** and **TAZ-BN**, the dominant RISC and IC contributions arise specifically from the C–H stretching modes on the phenyl ring adjacent to the seven-membered heterocyclic ring. In contrast, for **PXZ-BN** and **DABNA-1**, the most influential vibrations correspond to the C–H stretching modes adjacent to the standard fused six-membered rings. These results suggest that the local chemical environment and the specific fusion topology of the boron–nitrogen (BN) framework significantly dictate the localization of non-radiative activity.

The results further emphasize that efficient TADF emitters require an asymmetric vibronic profile. Ideally, the IC-related vibrational activity should remain sufficiently weak and localized to suppress exciton quenching and preserve a high photoluminescence quantum yield, whereas the RISC-active modes should retain sufficiently strong vibronic coupling to facilitate efficient triplet harvesting. In this regard, **DTBA-BN2** successfully suppresses RISC activity but at the cost of extremely weak spin-vibronic coupling, which limits efficient triplet upconversion. By contrast, **TAZ-BN** achieves a more favorable balance, simultaneously maintaining relatively controlled IC contributions while strongly enhancing RISC activity. **PXZ-BN** and **DABNA-1** exhibit intermediate behavior, where broader vibrational manifolds contribute to both IC and spin–flip processes. Taken together, the combined coupling–rate representation provides a substantially more transparent physical picture of how individual vibrational modes govern excited-state relaxation pathways in MR-TADF emitters.

To identify the regime in which semiclassical and fully quantum-mechanical treatments yield reliable and consistent predictions, we compared the corresponding RISC rate constants, as shown in Fig. 5. In this figure, the solid curves represent the fully quantum-mechanical results, whereas the dashed curves correspond to the semiclassical Marcus formalism. The comparison was performed for three representative reorganization energies, λ = 0.05, 0.10, and 0.15 eV, values that are typical for MR-TADF emitters. Larger reorganization energies were not considered, since λ for rigid MR-TADF systems generally remains below approximately 0.2 eV. Beyond this range, substantial deviations between semiclassical and quantum-mechanical descriptions are expected.

A detailed analysis reveals a clear dependence on the magnitude of the reorganization energy. For λ = 0.05 eV, the semiclassical Marcus expression slightly overestimates the RISC rate, particularly in the small-ΔE_{ST} regime. At λ = 0.10 eV, however, the agreement becomes remarkably good, with the semiclassical rates only marginally underestimating the fully quantum-mechanical values. Upon further increasing the reorganization energy to 0.15 eV, the discrepancy between the two approaches grows noticeably, reflecting the increasing importance of quantum vibronic effects in systems with larger structural relaxation.

These results indicate that $\lambda \approx 0.10$ eV represents an optimal regime in which the semiclassical Marcus formalism provides an excellent approximation to the full quantum-mechanical treatment for MR-TADF emitters. This finding is particularly valuable, as it delineates the practical limits of the widely used Marcus framework for predicting RISC kinetics in rigid organic emitters. More broadly, the performance of a TADF emitter is governed by the interplay among several competing rate constants, including the fluorescence rate, the non-radiative decay rate from the singlet state, the ISC rate, and the RISC rate. In particular, efficient TADF requires a careful balance between ISC and RISC: ISC must be sufficiently fast to populate the triplet manifold efficiently, while RISC must be rapid enough to upconvert triplet excitons back to the emissive singlet state before non-radiative triplet losses occur.

For completeness, the fully quantum-mechanical rate constants are summarized in Table 2. Among the four emitters, **TAZ-BN** exhibits the highest k_{RISC}, whereas **DTBA-BN2** shows the largest k_{ISC}. However, comparing these absolute rates in isolation can be misleading, as efficient TADF relies on a delicate balance between the forward and reverse intersystem

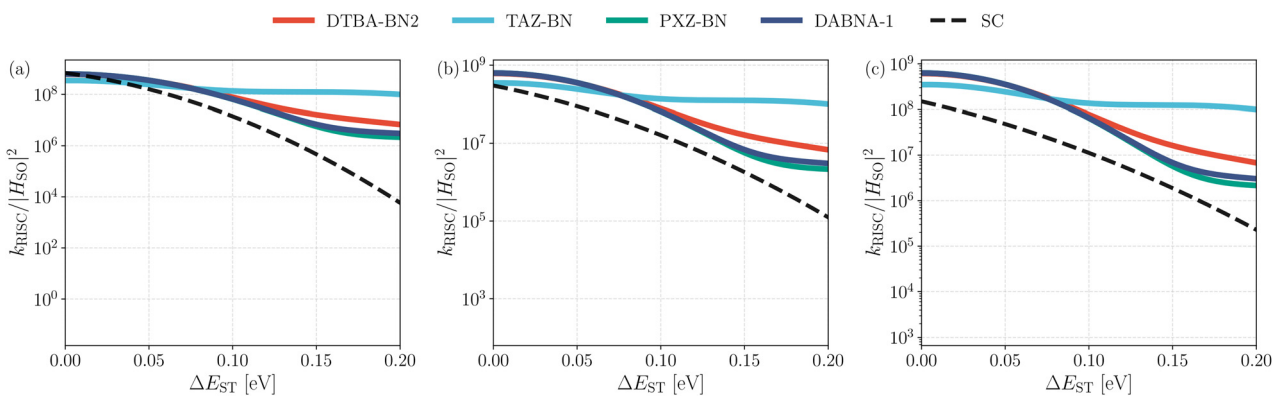


Fig. 5 Comparison of the fully quantum-mechanical (QM, solid lines) and semiclassical Marcus (SC, dashed lines) predictions of $k_{RISC}/|H_{SO}|^2$ as a function of ΔE_{ST} for representative reorganization energies relevant to MR-TADF emitters. The analysis highlights the regime in which the semiclassical approximation accurately reproduces the quantum-mechanical reverse intersystem crossing rates.

Table 2 Calculated intersystem crossing (k_{ISC}) and reverse intersystem crossing (k_{RISC}) rate constants, their ratio (k_{RISC}/k_{ISC}), and the oscillator strengths (f) of the lowest singlet excitation for the investigated MR-TADF emitters. All rate constants are reported in units of 10^6 s^{-1}

Compound	k_{ISC}	k_{RISC}	k_{RISC}/k_{ISC}	f
DTBA-BN2	20.1	0.128	0.006368	0.30
TAZ-BN	4.57	1.42	0.310722	0.07
PXZ-BN	2.90	0.00388	0.001338	0.33
DABNA-1	6.55	0.00273	0.000417	0.28

crossing processes. To better assess this balance, we therefore consider the ratio k_{RISC}/k_{ISC}, where a larger value signifies more efficient triplet harvesting and singlet regeneration. This metric is especially important for TADF materials because nearly 75% of electrically generated excitons are initially formed in the triplet manifold. Consequently, a higher k_{RISC}/k_{ISC} ratio directly translates into a greater likelihood of converting triplet excitons into emissive singlet states.

Analysis of the computed ratios clearly differentiates the four candidates. The poorest-performing molecule (**DABNA-1**) exhibits the smallest k_{RISC}/k_{ISC} value, followed by **PXZ-BN**, **DTBA-BN2**, and **TAZ-BN**, while **TAZ-BN** displays the largest ratio of 0.31. This indicates that **TAZ-BN** offers the most favorable balance between ISC and RISC among the investigated systems. Nevertheless, this ratio alone does not fully determine practical device performance. The oscillator strength (f), which governs the probability of radiative emission, is equally crucial. Although **TAZ-BN** possesses the highest k_{RISC}/k_{ISC} ratio, its oscillator strength is markedly smaller than that of the other compounds (Table 2). Indeed, its f value is the lowest in the series and is approximately one-fourth of those calculated for **DTBA-BN2**, **PXZ-BN**, and **DABNA-1**. As a result, the superior ISC/RISC balance of **TAZ-BN** is partially offset by its weak radiative character. In contrast, **DTBA-BN2** achieves a more attractive compromise, combining a reasonably large k_{RISC}/k_{ISC} ratio with a substantially higher oscillator strength. This balanced interplay between efficient triplet upconversion and strong radiative emission ultimately makes **DTBA-BN2** the most promising candidate among the molecules considered here.

A comparative analysis between conventional donor–acceptor (D–A) emitters and MR-TADF systems reveals fundamentally different roles of vibrational dynamics in governing non-radiative relaxation processes. For the IC pathway, both molecular classes exhibit broadly similar vibrational behavior because the $S_1 \rightarrow S_0$ transition proceeds through energetically accessible vibronic relaxation channels irrespective of molecular rigidity. Consequently, the mode-dependent characteristics of IC remain relatively comparable across both D–A and MR-TADF frameworks.

In contrast, pronounced differences emerge for the ISC and RISC processes. MR-TADF emitters possess rigid, fused, and highly constrained molecular frameworks that suppress large-amplitude torsional and low-frequency vibrational motions. Such rigidity limits the vibrational modulation necessary to effectively enhance spin–vibronic coupling, making the associated vibronic activation energetically less favorable. As a result, the ISC/RISC channels in MR-TADF systems generally exhibit very small electron–phonon coupling strengths together with comparatively weak transition rates.

Conversely, D–A type emitters contain flexible donor–acceptor linkages that readily support low-energy twisting and rotational motions around the interfragment bonds. These soft vibrational coordinates strongly facilitate spin-vibronic interactions, thereby promoting significantly larger vibronic coupling strengths in the ISC and RISC channels. Consequently, D–A architectures typically exhibit higher spin–flip transition rates than structurally rigid MR-TADF systems. Overall, while the IC process appears comparatively insensitive to molecular rigidity, the ISC/RISC dynamics are highly dependent on structural flexibility and vibrational adaptability, both of which are substantially more pronounced in D–A emitters than in MR-TADF frameworks.

The vibrational mode analysis presented here provides a practical framework for the rational design of high-efficiency emitters. By identifying vibrational modes that predominantly promote non-radiative decay pathways such as IC and ISC, or alternatively facilitate RISC, one can predict and tune exciton dynamics in newly designed molecules. Although complete decoupling of electronic transitions from vibrational activity remains challenging due to the simultaneous involvement of multiple modes, selective suppression of detrimental modes becomes feasible once the dominant contributions are identified. Such strategies have already been demonstrated in recent studies through enhanced structural rigidity and optimized molecular fusion patterns.[21]

The present analysis further highlights important molecular design principles. For example, although the seven-membered ring in **TAZ-BN** provides comparatively balanced ISC/RISC activity, its limited oscillator strength restricts overall performance, suggesting that directly fused seven-membered architectures may be more effective. Similarly, increasing molecular rigidity from **DABNA-1** to **PXZ-BN** improves the ISC/RISC balance while simultaneously suppressing non-radiative decay channels, thereby enhancing emission efficiency.

While the present work focuses on second-period heteroatoms (O, N) to isolate framework-topology effects, extending these vibronic principles to heavier chalcogens (S, Se, Te) highlights an important physical trade-off.[46] Because spin–orbit coupling matrix elements scale approximately with Z^2, heavy-atom substitution substantially accelerates intrinsic k_{ISC} and k_{RISC} rates. Simultaneously, the heavier atomic mass shifts vibrational modes toward lower frequencies, thereby increasing the total reorganization energy (λ) and enhancing non-radiative relaxation channels. For heavy-atom MR-TADF emitters, efficient harvesting requires that SOC enhancement dominates over these added low-frequency vibrational losses—a promising direction currently being explored in ongoing follow-up work.

4 Conclusion

We have carried out a comprehensive mode-resolved computational investigation of the vibrational contributions governing

 This journal is © the Owner Societies 2026

the excited-state dynamics of four structurally related MR-TADF emitters. Across all systems, the Huang–Rhys factors decrease systematically with increasing vibrational mode number, revealing a clear separation of vibronic roles: low-frequency, delocalized vibrations predominantly facilitate the spin-allowed internal conversion process, whereas high-frequency, localized modes primarily mediate the spin-forbidden ISC and RISC channels. Consistent with this picture, IC is associated with larger Huang–Rhys factors and greater reorganization energies than either ISC or RISC, reflecting the more substantial nuclear reorganization accompanying singlet-to-ground-state relaxation.

Our mode-resolved electron–phonon coupling analysis further demonstrates that the most significant vibronic contributions originate from vibrations in the 500–1600 cm^{-1} region, corresponding mainly to skeletal stretching and in-plane bending motions of the fused aromatic framework. Among the molecules studied, **DTBA-BN2** emerges as particularly noteworthy. It exhibits a highly selective vibronic profile, characterized by a single dominant IC-coupled mode and unusually high-frequency ISC/RISC-active vibrations. As a consequence, **DTBA-BN2** possesses the smallest effective Huang–Rhys factor (S_{eff}) for spin–flip transitions, a large oscillator strength (f = 0.30), and the best experimentally reported external quantum efficiency. In contrast, **TAZ-BN** displays the most favorable balance between reverse and forward intersystem crossing, with a k_{RISC}/k_{ISC} ratio of 0.31. However, its substantially reduced oscillator strength (f = 0.07) limits its overall emissive performance, highlighting that an optimal ISC/RISC balance alone does not guarantee superior TADF efficiency.

A direct comparison between fully quantum-mechanical and semiclassical Marcus predictions for k_{RISC} identifies a reorganization energy of approximately $\lambda \approx 0.10$ eV as the regime where both approaches yield excellent agreement. At smaller reorganization energies, however, the Marcus formalism systematically overestimates the RISC rate, emphasizing the need for caution when applying semiclassical treatments to low-reorganization-energy MR-TADF systems.

Taken together, these results establish three key vibronic design principles for next-generation high-performance MR-TADF emitters: (i) minimize IC and ISC losses by restricting the number of strongly coupled vibrational modes; (ii) selectively promote RISC through targeted coupling to high-frequency spin–flip-active vibrations; and (iii) preserve a large oscillator strength to ensure efficient radiative decay. Finally, the effective descriptors introduced in this work—S_{eff}, ν_{eff}, and the mode-resolved vibronic coupling spectra—provide a robust and computationally efficient framework for the rational screening and molecular engineering of narrowband MR-TADF emitters for advanced OLED applications.

Author contributions

AM conceived the problem. Sanyam conducted all the simulations. Sanyam and AM analyzed the results and prepared the draft.

Conflicts of interest

There are no conflicts to declare.

Data availability

The data that support the findings of this study are available from the corresponding authors upon reasonable request.

Supplementary information (SI): the supplementary information contains methodology for computing non-radiative rates, experimentally measured ΔE_{ST} and EQE, mode-to-frequency mapping, mode-resolved infrared (IR) spectra, mode-resolved vibrational reorganization energies, and representative vibrational modes. See DOI: https://doi.org/10.1039/d6cp02133f.

Acknowledgements

The authors gratefully acknowledge the Indian Institute of Technology Gandhinagar, India, for providing research facilities and financial support. We thank PARAM Ananta for computational resources.

References

1 H. Uoyama, K. Goushi, K. Shizu, H. Nomura and C. Adachi, Highly efficient organic light-emitting diodes from delayed fluorescence, *Nature*, 2012, **492**, 234–238.
2 Y. Liu, C. Li, Z. Ren, S. Yan and M. R. Bryce, All-organic thermally activated delayed fluorescence materials for organic light-emitting diodes, *Nat. Rev. Mater.*, 2018, **3**, 1–20.
3 A. Endo, K. Sato, K. Yoshimura, T. Kai, A. Kawada, H. Miyazaki and C. Adachi, Efficient up-conversion of triplet excitons into a singlet state and its application for organic light emitting diodes, *Appl. Phys. Lett.*, 2011, **98**, 083302.
4 K. Goushi, K. Yoshida, K. Sato and C. Adachi, Organic light-emitting diodes employing efficient reverse intersystem crossing for triplet-to-singlet state conversion, *Nat. Photonics*, 2012, **6**, 253–258.
5 Y. Xu, C. Li, Z. Li, Q. Wang, X. Cai, J. Wei and Y. Wang, Constructing Charge- Transfer Excited States Based on Frontier Molecular Orbital Engineering: Narrowband Green Electroluminescence with High Color Purity and Efficiency, *Angew. Chem.*, 2020, **59**, 17442–17446.
6 P. Stachelek, J. S. Ward, P. L. dos Santos, A. Danos, M. Colella, N. Haase, S. J. Raynes, A. S. Batsanov, M. R. Bryce and A. P. Monkman, Molecular Design Strategies for Color Tuning of Blue TADF Emitters, *ACS Appl. Mater. Interfaces*, 2019, **11**, 27125–27133.
7 Y. Zhang, D. Zhang, J. Wei, X. Hong, Y. Lu, D. Hu, G. Li, Z. Liu, Y. Chen and L. Duan, Achieving pure green electroluminescence with CIEy of 0.69 and EQE of 28.2% from an aza-fused multi-resonance emitter, *Angew. Chem.*, 2020, **132**, 17652–17656.
8 T. Hatakeyama, K. Shiren, K. Nakajima, S. Nomura, S. Nakatsuka, K. Kinoshita, J. Ni, Y. Ono and T. Ikuta,

Ultrapure Blue Thermally Activated Delayed Fluorescence Molecules: Efficient HOMO-LUMO Separation by the Multiple Resonance Effect, *Adv. Mater.*, 2016, **28**, 2777–2781.
9 Sanyam, R. Khatua and A. Mondal, Constructing Multiresonance Thermally Activated Delayed Fluorescence Emitters for Organic LEDs: A Computational Investigation, *J. Phys. Chem. A*, 2023, **127**, 10393–10405.
10 R. Nikhitha and A. Mondal, Breaking the trade-off between and oscillator strength in hybrid LR/SR-CT compounds for enhanced TADF performance, *J. Mater. Chem. C*, 2025, **13**, 1893–1906.
11 T. J. Penfold, E. Gindensperger, C. Daniel and C. M. Marian, Spin-vibronic mechanism for intersystem crossing, *Chem. Rev.*, 2018, **118**, 6975–7025.
12 X.-K. Chen, D. Kim and J.-L. Bredas, Thermally activated delayed fluorescence (TADF) path toward efficient electroluminescence in purely organic materials: molecular level insight, *Acc. Chem. Res.*, 2018, **51**, 2215–2224.
13 P. S. Rukin, M. Fortino, D. Prezzi and C. A. Rozzi, Complementing Adiabatic and Nonadiabatic Methods To Understand Internal Conversion Dynamics in Porphyrin Derivatives, *J. Chem. Theory Comput.*, 2024, **20**, 10759–10769.
14 J. Guan, C. Shen, J. Peng and J. Zheng, What leads to aggregation-induced emission, *J. Phys. Chem. Lett.*, 2021, **12**, 4218–4226.
15 H. S. Kim, S. H. Lee, S. Yoo and C. Adachi, Understanding of complex spin upconversion processes in charge-transfer-type organic molecules, *Nat. Commun.*, 2024, **15**, 2267.
16 M. Yang, I. S. Park and T. Yasuda, Full-Color, Narrowband, and High-Efficiency Electroluminescence from Boron and Carbazole Embedded Polycyclic Heteroaromatics, *J. Am. Chem. Soc.*, 2020, **142**, 19468–19472.
17 D. Hall, S. M. Suresh, P. L. dos Santos, E. Duda, S. Bagnich, A. Pershin, P. Rajamalli, D. B. Cordes, A. M. Z. Slawin, D. Beljonne, A. Kohler, I. D. W. Samuel, Y. Olivier and E. Zysman-Colman, Improving Processability and Efficiency of Resonant TADF Emitters: A Design Strategy, *Adv. Opt. Mater.*, 2020, **8**, 1901627.
18 D. Hall, J. C. Sancho-Garcıa, A. Pershin, G. Ricci, D. Beljonne, E. Zysman-Colman and Y. Olivier, Modeling of multiresonant thermally activated delayed fluorescence emitters properly accounting for electron correlation is key, *J. Chem. Theory Comput.*, 2022, **18**, 4903–4918.
19 D. Hall, J. C. Sancho-Garcia, A. Pershin, D. Beljonne, E. Zysman-Colman and Y. Olivier, Benchmarking DFT functionals for excited-state calculations of donor–acceptor TADF emitters: insights on the key parameters determining reverse intersystem crossing, *J. Phys. Chem. A*, 2023, **127**, 4743–4757.
20 F. Huang, K. Wang, Y.-Z. Shi, X.-C. Fan, X. Zhang, J. Yu, C.-S. Lee and X.-H. Zhang, Approaching Efficient and Narrow RGB Electroluminescence from D–A-Type TADF Emitters Containing an Identical Multiple Resonance Backbone as the Acceptor, *ACS Appl. Mater. Interfaces*, 2021, **13**, 36089–36097.
21 P. Ghosh, A. M. Alvertis, R. Chowdhury, P. Murto, A. J. Gillett, S. Dong, A. J. Sneyd, H.-H. Cho, E. W. Evans, B. Monserrat, L. Feng, S. Christoph, B. Hugo, H. F. Richard and R. Akshay, Decoupling excitons from high-frequency vibrations in organic molecules, *Nature*, 2024, **629**, 355–362.
22 T. Pizza, A. Capobianco and A. Troisi, The importance of high-frequency modes in the prediction of RISC rates for TADF molecules, *J. Phys. Chem. Lett.*, 2025, **16**, 3056–3062.
23 D. Valverde, C. T. Ser, G. Ricci, K. Jorner, R. Pollice, A. Aspuru-Guzik and Y. Olivier, Computational Investigations of the Detailed Mechanism of Reverse Intersystem Crossing in Inverted Singlet–Triplet Gap Molecules, *ACS Appl. Mater. Interfaces*, 2024, **16**, 66991–67001.
24 Sanyam and A. Mondal, Decoding vibrational contributions and exciton dynamics in TADF emitters for enhanced OLED efficiency, *ACS Appl. Electron. Mater.*, 2025, **7**, 4843–4854.
25 R. Huang, J. Avo, T. Northey, E. Chaning-Pearce, P. L. Dos Santos, J. S. Ward, P. Data, M. K. Etherington, M. A. Fox and T. J. Penfold, The contributions of molecular vibrations and higher triplet levels to the intersystem crossing mechanism in metal-free organic emitters, *J. Mater. Chem. C*, 2017, **5**, 6269–6280.
26 R. Damari, O. Weinberg, D. Krotkov, N. Demina, K. Akulov, A. Golombek, T. Schwartz and S. Fleischer, Strong coupling of collective intermolecular vibrations in organic materials at terahertz frequencies, *Nat. Commun.*, 2019, **10**, 3248.
27 D. R. Zahn, G. N. Gavrila and G. Salvan, Electronic and vibrational spectroscopies applied to organic/inorganic interfaces, *Chem. Rev.*, 2007, **107**, 1161–1232.
28 O. P. Dimitriev, Dynamics of excitons in conjugated molecules and organic semiconductor systems, *Chem. Rev.*, 2022, **122**, 8487–8593.
29 K. R. Naveen, J. H. Oh, H. S. Lee and J. H. Kwon, Tailoring extremely narrow FWHM in hypsochromic and bathochromic shift of polycyclo-heteraborin MR-TADF materials for high-performance OLEDs, *Angew. Chem.*, 2023, **135**, e202306768.
30 X. Lv, J. Miao, M. Liu, Q. Peng, C. Zhong, Y. Hu, X. Cao, H. Wu, Y. Yang and C. Zhou, Extending the π-skeleton of multi-resonance TADF materials towards high-efficiency narrowband deep-blue emission, *Angew. Chem., Int. Ed.*, 2022, **61**, e202201588.
31 H. Nemma, Y. Kori, N. Meguro, R. Mimura, Y. Chiba, J. Kido and H. Sasabe, π-Extended Phenoxazine-Based Asymmetric MR-TADF Emitters for Narrow Emission Band Green OLEDs with a Power Efficiency of 150 lm W^{-1}, an EQE of 27%, and an LT95 of Over 3000 h at 1000 cd m^{-2}, *Adv. Opt. Mater.*, 2025, **13**, 2402131.
32 Y.-K. Chen, J. Lei and T.-L. Wu, Elevating the upconversion performance of a multiple resonance thermally activated delayed fluorescence emitter via an embedded azepine approach, *Chem. Sci.*, 2024, **15**, 10146–10154.
33 M. Mamada, M. Hayakawa, J. Ochi and T. Hatakeyama, Organoboron-based multipleresonance emitters: synthesis, structure–property correlations, and prospects, *Chem. Soc. Rev.*, 2024, **53**, 1624–1692.
34 M. J. Frisch, G. W. Trucks, H. B. Schlegel, G. E. Scuseria, M. A. Robb, J. R. Cheeseman, G. Scalmani, V. Barone,

 This journal is © the Owner Societies 2026

B. Mennucci, G. A. Petersson, H. Nakatsuji, M. Caricato, X. Li, H. P. Hratchian, A. F. Izmaylov, J. Bloino, G. Zheng, J. L. Sonnenberg, M. Hada, M. Ehara, K. Toyota, R. Fukuda, J. Hasegawa, M. Ishida, T. Nakajima, Y. Honda, O. Kitao, H. Nakai, T. Vreven, J. A. Montgomery, J. E. Peralta, F. Ogliaro, M. Bearpark, J. J. Heyd, E. Brothers, K. N. Kudin, V. N. Staroverov, R. Kobayashi, J. Normand, K. Raghavachari, A. Rendell, J. C. Burant, S. S. Iyengar, J. Tomasi, M. Cossi, N. Rega, J. M. Millam, M. Klene, J. E. Knox, J. B. Cross, V. Bakken, C. Adamo, J. Jaramillo, R. Gomperts, R. E. Stratmann, O. Yazyev, A. J. Austin, R. Cammi, C. Pomelli, J. W. Ochterski, R. L. Martin, K. Morokuma, V. G. Zakrzewski, G. A. Voth, P. Salvador, J. J. Dannenberg, S. Dapprich, A. D. Daniels, Ö. Farkas, J. B. Foresman, J. V. Ortiz, J. Cioslowski and D. J. Fox, *Gaussian 09, Revision E.01*, Gaussian Inc., Wallingford CT, 2009.

35 F. Neese, The ORCA program system, *WIREs Comput. Mol. Sci.*, 2012, **2**, 73–78.

36 E. Bremond and C. Adamo, Seeking for parameter-free double-hybrid functionals: The PBE0-DH model, *J. Chem. Phys.*, 2011, **135**, 024106.

37 C. Adamo and V. Barone, Toward reliable density functional methods without adjustable parameters: The PBE0 model, *J. Chem. Phys.*, 1999, **110**, 6158–6170.

38 P.-F. Loos and D. Jacquemin, Evaluating 0–0 energies with theoretical tools: A short review, *ChemPhotoChem*, 2019, **3**, 684–696.

39 A. Togo, L. Chaput and I. Tanaka, Distributions of phonon lifetimes in Brillouin zones, *Phys. Rev. B:Condens. Matter Mater. Phys.*, 2015, **91**, 094306.

40 A. Seko, A. Togo, H. Hayashi, K. Tsuda, L. Chaput and I. Tanaka, Prediction of lowthermal-conductivity compounds with first-principles anharmonic lattice-dynamics calculations and Bayesian optimization, *Phys. Rev. Lett.*, 2015, **115**, 205901.

41 Sanyam, N. Tejiyan, K. Singh and A. Mondal, Is range separation always necessary for modeling TADF emitters? A benchmark study of B3LYP on dispersion-corrected geometries vs. tuned ωB97X-D, *Phys. Chem. Chem. Phys.*, 2026, **28**, 16011–16024.

42 D. Jacquemin, E. A. Perpete, I. Ciofini, C. Adamo, R. Valero, Y. Zhao and D. G. Truhlar, On the performances of the M06 family of density functionals for electronic excitation energies, *J. Chem. Theory Comput.*, 2010, **6**, 2071–2085.

43 Sanyam, R. Khatua and A. Mondal, Cost-Effective Approach for Modeling of Multiresonant Thermally Activated Delayed Fluorescence Emitters, *J. Chem. Theory Comput.*, 2023, **19**, 9290–9301.

44 Y. Takano and K. Houk, Benchmarking the conductor-like polarizable continuum model (CPCM) for aqueous solvation free energies of neutral and ionic organic molecules, *J. Chem. Theory Comput.*, 2005, **1**, 70–77.

45 I. E. Serdiuk, M. Monka, K. Kozakiewicz, B. Liberek, P. Bojarski and S. Y. Park, Vibrationally assisted direct intersystem crossing between the same charge-transfer states for thermally activated delayed fluorescence: analysis by marcus–hush theory including reorganization energy, *J. Phys. Chem. B*, 2021, **125**, 2696–2706.

46 X. Suo, Z. Yang, G.-X. Yang, R. Wang, Y. Zhang, Z. Mahmood, Y. Huo, S.-J. Su and S. Ji, Intramolecular Hydrogen-Bonding-Rigidified Boron-Dipyrromethene Dimers for Narrowband Near-Infrared OLEDs, *Adv. Opt. Mater.*, 2026, e71605.